Originally published as:

RESEARCH ARTICLE

Key Points:
- Terraces on Olympus Mons volcano (Mars) are explained as thrust faults
- Gravity flexure in combination with spreading can account for Olympus Mons' structural arrangement
- A low friction at the edifice base could lead to scarp formation and collapse

Supporting Information:
- Text S1 and Captions of Movies S1 and S2
- Movie S1
- Movie S2

Correspondence to:
S. Musiol,
stefanie.musiol@fu-berlin.de

Lithospheric flexure and gravity spreading of Olympus Mons volcano, Mars

S. Musiol[1], E. P. Holohan[2], B. Cailleau[3], T. Platz[1,4,5], A. Dumke[1], T. R. Walter[2], D. A. Williams[6], and S. van Gasselt[1]

[1]Planetary Sciences and Remote Sensing, Institute of Geological Sciences, Freie Universität Berlin, Berlin, Germany, [2]Physics of Earthquakes and Volcanoes, GFZ German Research Centre for Geosciences, Potsdam, Germany, [3]Geophysics, Institute of Geological Sciences, Freie Universität Berlin, Berlin, Germany, [4]Planetary Science Institute, Tucson, Arizona, USA, [5]Max Planck Institute for Solar System Research, Göttingen, Germany, [6]Ronald Greeley Center for Planetary Studies, School of Earth and Space Exploration, Arizona State University, Tempe, Arizona, USA

Abstract The structural architecture of large volcanoes is governed substantially by gravity-driven deformation that is manifest as distinct processes such as basement flexure or volcanic spreading. Temporal effects and the mutual interplay of these processes have been investigated only to a limited extent, and so we present novel numerical models of the time-dependent deformation associated with them. The models simulate the combined effects of lithospheric flexure and volcanic spreading during growth increments of an elastoplastic volcanic cone. Different spreading scenarios are considered by a variable coupling decoupling behavior at the interface between volcano and basement. We apply our models to Olympus Mons on Mars, which is characterized by upper to middle flank terraces on the shield, is encircled by a basal scarp that has an average slope of 30° and is surrounded by distant deposits that resemble large-scale slumping features on Earth. Our results are consistent with the interpretation that terraces on Olympus Mons' flanks form by thrust faulting that results from lithospheric flexure. The presence and expression of terraces depend on the coupling of volcano and basement, on the time of volcano growth relative to mantle relaxation, and on the cohesion of the edifice. The encircling scarp may be related to a very low friction detachment at the edifice base, which leads to a normal fault regime on the lowermost flanks. With time and volcano growth, predicted stress and faulting regimes migrate only slightly, indicating that the structural architecture of volcanoes is largely set in the very early stages of formation.

1. Introduction

Volcanoes develop particular structures and morphologies due to a variety of processes, including magma emplacement and migration, hydrothermal activity, landsliding, tectonic faulting, lithospheric flexure, and gravitational spreading [*Dzurisin*, 2007]. Large and tall volcanoes, in particular, are thought to be governed by gravity-driven deformation [*Borgia et al.*, 2000]. This form of deformation results in an outward movement along a basal detachment, termed spreading, and/or a downflexing of the underlying basement or lithosphere [*Byrne et al.*, 2013]. In this paper, we investigate the mutual effects of gravitational spreading and lithospheric flexure for the largest volcano known in the Solar System: Olympus Mons on Mars. An improved understanding of Olympus Mons is useful to understanding large volcanoes in general. This is, on the one hand, because of its enormous size which is a consequence of the lack of plate tectonics on Mars and of a long-lived magma feeding source and, on the other hand, because it has preserved its volcano-tectonic history over billions of years.

1.1. Olympus Mons: Morphological Characteristics, Lithospheric Loading, and Gravity Tectonics

Olympus Mons is situated in the northern hemisphere of Mars, west of the Tharsis Volcanic Province (Figure 1). It is a basaltic shield volcano with a relief of 22 km, an extent of 840 × 640 km including its scarp-draping lava flows, and an average flank slope of 5° [*Plescia*, 2004]. A circumferential scarp with a height of several kilometers encloses the main shield, which is approximately 600 km in diameter. This scarp is spatially and genetically associated with lobate aureoles of grooved terrain surrounding the volcano [*Harris*, 1977]; these aureoles were probably formed by mass movement [*Lopes et al.*, 1980, 1982].

Olympus Mons represents a considerable gravitational load on the Martian lithosphere, with a large free-air gravity anomaly and a positive Bouger anomaly resolvable at a scale of 300 km [*Neumann et al.*, 2004]. Due to
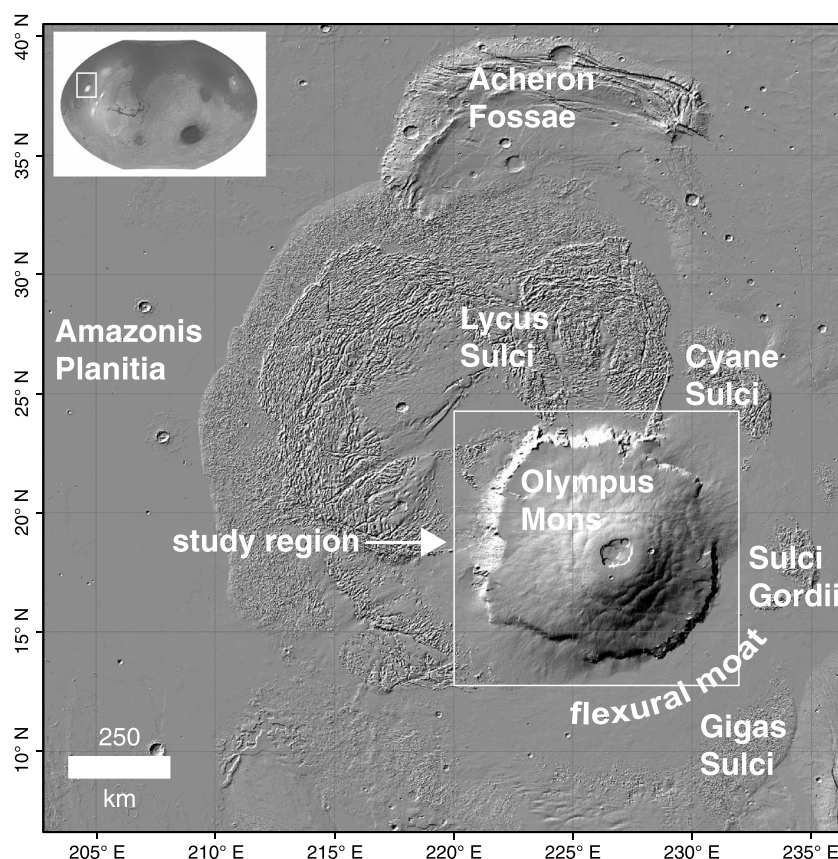
Figure 1. Mars Orbiter Laser Altimeter shaded relief in cylindrical equidistant projection of Olympus Mons and the surrounding plains. A global Mars base map is shown in the upper left corner in Robinson projection for context. Olympus Mons is bordered by the Tharsis Volcanic Province to the southeast and by Amazonis Planitia to the west. The volcano is surrounded by lobate aureoles (Sulci), possibly formed by landslides.

its load, the volcano downflexed the underlying lithosphere, which is evident by the presence of an encircling flexural moat thought to be mostly filled by lava and landslide deposits (Figure 1) [e.g., *Isherwood et al.*, 2013, *McGovern et al.*, 2014].

Prominent terrace-like morphotectonic features on Olympus Mons' shield have been hypothesized to be the result of lithospheric flexure. *Carr et al.* [1977] first observed a concentric pattern of such terraces on the upper flanks of the shield. *Thomas et al.* [1990] later showed that terraces are observed not only on Olympus Mons but also on the Tharsis Montes (Arsia Mons, Pavonis Mons, and Ascraeus Mons). *Byrne et al.* [2009] characterized the volcano flank terraces as convex upward features arranged in an imbricate stacking pattern, and they reported such terraces to be present on several other large basaltic volcanoes on Mars and Earth (e.g., also on Alba Patera, Elysium Mons, and Mauna Loa). These terraces have been interpreted as the surface expressions of thrust faults that have been generated by elastic self-deformation of the volcanic cone [*Thomas et al.*, 1990]. The interpretation is still valid, but the formation mechanism is rather basement flexure, as shown by numerical and analog models that produced radial compression and concentric terrace-like structures on the upper volcano flanks [*McGovern and Solomon*, 1993; *Byrne et al.*, 2013].

In contrast, the basal scarp and aureole deposits of Olympus Mons have been interpreted as the results of gravitational sliding, thrusting, and spreading [*Harris*, 1977; *Lopes et al.*, 1980, 1982; *Francis and Wadge*, 1983]. *Tanaka* [1985] showed with geomorphologic analyses and rheologic modeling that widespread detachment sliding could have occurred along a basal layer containing interstitial ice. On the basis of comparison with analogs on Earth such as Hawaii, *Borgia et al.* [1990, 2000] claimed that Olympus Mons has undergone volcanic spreading by thrusting of the lower flanks. *Lopes et al.* [1980, 1982] introduced the idea of a mass movement origin for the aureole deposits, a hypothesis further developed by *McGovern et al.* [2004a]. With numerical simulations of volcanoes with low basal friction, *Morgan and McGovern* [2005] and *McGovern and Morgan* [2009]

concluded that subsurface zones of weakness (clay-rich sediments) can induce lateral spreading and over-thrusting of the edifice and that these basal weak zones likely contributed to the formation of the scarp and aureole deposits. *De Blasio* [2011], however, argued for the aureole deposits as a consequence of submarine landslides on the basis of comparison with Earth analogs and numerical modeling of hydroplaning.

1.2. Aim of This Work

Observed morphotectonic features both on the shield and in the vicinity of the volcano hint to diverse deformational processes at Olympus Mons. Nevertheless, few studies have addressed the interplay of these processes quantitatively. For example, former analytical models of flexure theory considered displacements and stresses due to flexure only for the lithosphere but not inside the volcano edifice [*Thurber and Toksöz*, 1978; *Comer et al.*, 1985]. In particle dynamics simulations, the effect of spreading alone without flexure was used to explain the structural characteristics of large volcanoes [*Morgan and McGovern*, 2005; *McGovern and Morgan*, 2009]. Although an earlier finite element study [*McGovern and Solomon*, 1993] as well as recent analog model results [*Byrne et al.*, 2013] suggested that a combination of lithospheric flexure and volcanic spreading best accounts for the evolution of Olympus Mons, this hypothesis has not been further elaborated with numerical methods that incorporate more realistic nonelastic edifice behavior. One primary advantage of numerical methods is the direct scaling to natural dimensions in comparison with the scaling ratios used in analog models [*Merle and Borgia*, 1996; *Oehler et al.*, 2005; *Delcamp et al.*, 2008; *Byrne et al.*, 2013].

In a more holistic approach, we investigate the time-dependent deformation of a volcanic cone under Martian gravity with finite element models that take into account the combined effects of lithospheric flexure and volcanic spreading. The novelty of this study includes variable basal detachment characteristics and a more realistic elastoplastic rheology, which enables fault expression and orientation to be better visualized and analyzed.

2. Observations and Evolutionary History of Olympus Mons

2.1. Structural Features

Mapping of Olympus Mons by *Morris and Tanaka* [1994] revealed an extensively faulted edifice, covered by lava channels [*Bleacher et al.*, 2007]. The main structural and morphologic features of Olympus Mons include upper to middle flank terraces, lower flank radial scarps, a basal circumferential scarp, and a summit caldera complex up to 90 km in diameter and up to 3 km deep with six nested calderas (1 in Figure 2a). The most detailed morphological map of terraces on Olympus Mons was derived by slope map analysis and revealed that the terraces form an imbricate pattern [*Byrne et al.*, 2013]. Although terraces occur on the upper flanks (2 in Figure 2a), concentric graben and troughs cut the lower flanks (3 in Figure 2a) and denote radial extension there. For the basal scarp we measured heights of up to 9 km in places. It has a slope of about 30° and is most pronounced along the northwestern and southeastern edges of the volcano (4 in Figure 2a). The scarp is superposed by lava flows in the northeast and southwest (5 in Figure 2a), leading to a reduction in slope angle (see Figure 2b). Remnant, elevated blocks, and radially oriented scarps on the lower flanks (6 in Figure 2a) have been interpreted as tear faults (i.e., strike-slip faults) [*Borgia et al.*, 1990].

2.2. Temporal Evolution

Model ages of Olympus Mons and its surroundings were derived by various authors from crater size-frequency measurements (for a method review see *Hartmann and Neukum* [2001] and *Platz et al.* [2013]). The oldest ages of 3.0–3.8 Ga were determined for some elevated blocks on the lower western flank of Olympus Mons [*Neukum et al.*, 2004; *Basilevsky et al.*, 2005]. The aureole deposits were emplaced in several stages and superpose each other [*Hiller et al.*, 1982; *Morris and Tanaka*, 1994; *De Blasio*, 2011]. *Hiller et al.* [1982] determined aureole model ages of 3.1–3.7 Ga, whereas recent mapping efforts [*Tanaka et al.*, 2014] assigned them an Amazonian formation age (younger than 3.4 Ga). From paleotopography and flexural modeling, *Isherwood et al.* [2013] calculated a time period of 1.13 (+0.74/−0.65) Ga for the formation of the majority of Olympus Mons. The volcano itself would have existed before 2.54 (+0.55/−0.69) Ga, which is the age for the northern aureole deposit inferred to postdate the bulk of volcano construction [*Isherwood et al.*, 2013]. Younger model ages of 100–450 Ma reported by *Neukum et al.* [2004], *Basilevsky et al.* [2005], and *Basilevsky et al.* [2006] for the caldera and for the eastern and western flanks could correspond to late-stage lava flows emplaced after the completion of most of the main shield.

Clearly, relatively late-stage lava eruptions obscure the bulk shield-building phase which appears to be of much shorter duration than the measured period of activity spanning almost 3.8 billion years. Consequently,
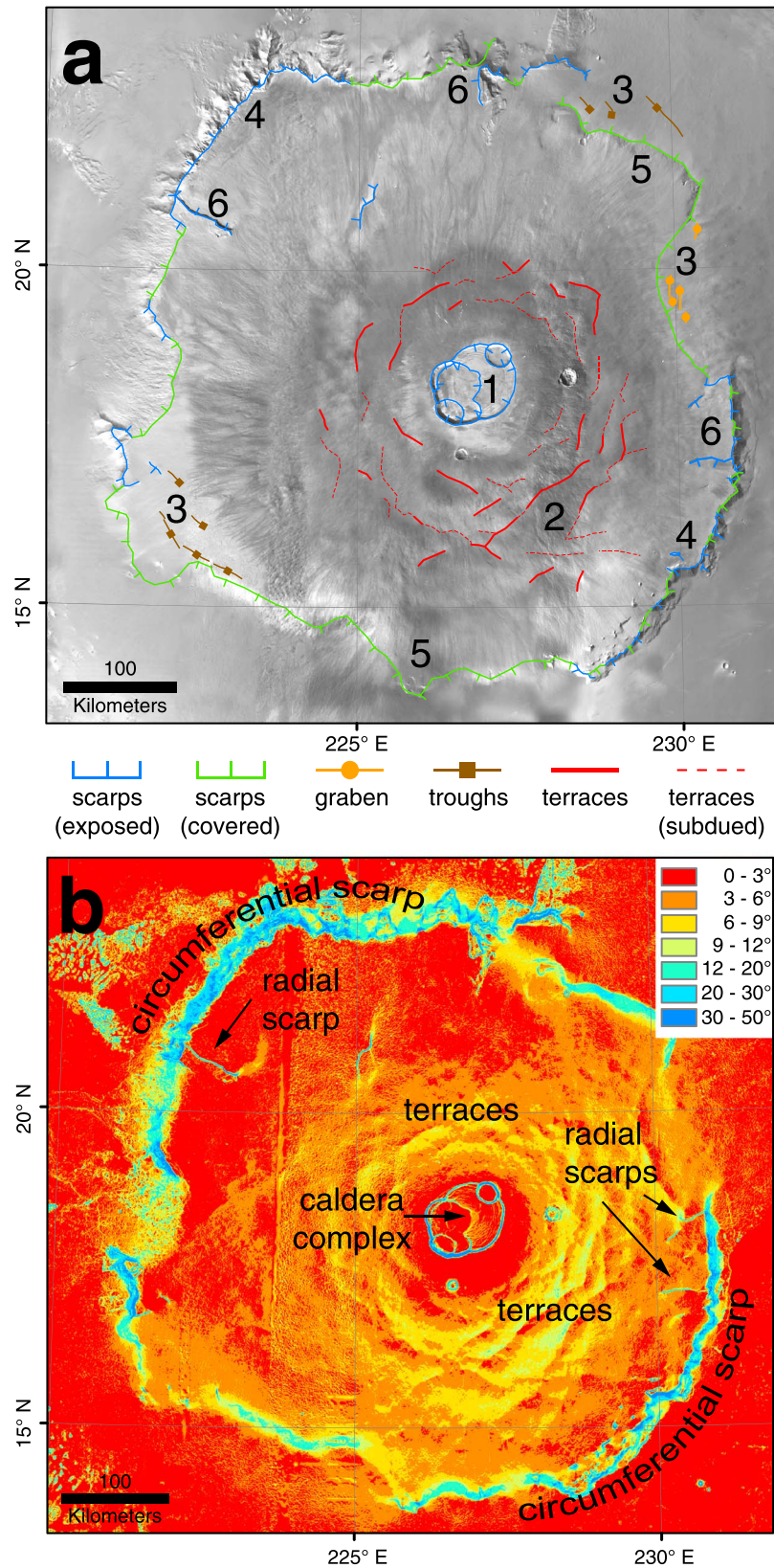
Figure 2. Maps of Olympus Mons in Mars Transverse Mercator projection. (a) Simplified morphologic map of Olympus Mons on a High Resolution Stereo Camera (HRSC) nadir mosaic; numbers are referred to in the text. (b) Slope map of Olympus Mons calculated from an HRSC digital elevation model.
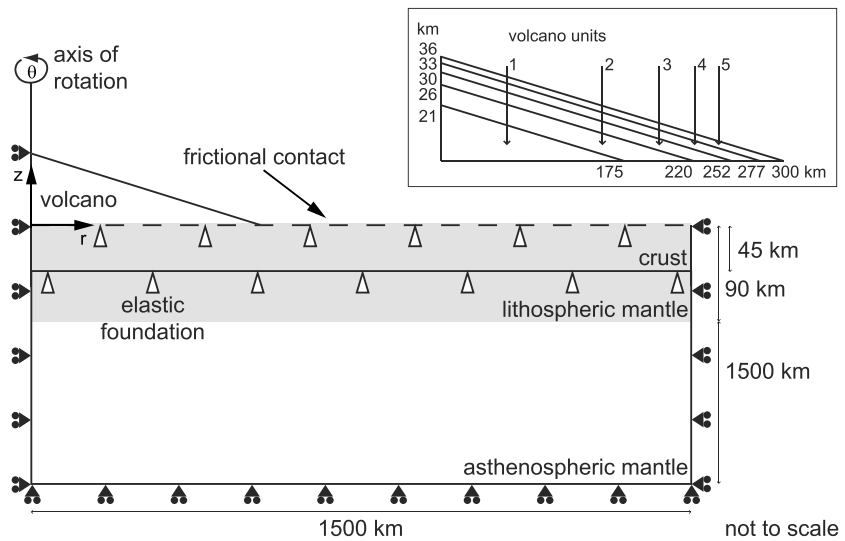
Figure 3. The axisymmetric model setup used in this study. The model consists of volcano, crust, lithospheric mantle, and asthenospheric mantle, with the dimensions for each given. The grey area denotes the lithosphere. Boundary conditions are indicated. Box at top right illustrates geometry and dimensions for the growing load.

for modeling purposes, we considered the growth time of the volcano in relation to the time in which the viscous mantle would respond to the load.

3. Model Setup

3.1. Geometric Setup

We performed finite element modeling with the commercial software ABAQUS (Dassault Systèmes Simulia Corp.). The two-dimensional axisymmetric model geometry consisted of four parts: the volcanic cone, the crust, the lithospheric mantle, and the asthenospheric mantle (Figure 3). The vertical and horizontal model dimensions of 1500 km ensured that no boundary effects would apply to the area of study. The radius of the volcanic cone was set to 300 km, based on an average observed diameter of the main shield of 600 km.

The final topographic height of a volcano after gravity-driven deformation depends on the thickness and material properties of the lithosphere, on the coupling of volcano and lithosphere, on the load density, and on the timescale of loading [*Thurber and Toksöz*, 1978; *McGovern and Solomon*, 1993]. Our test models proved that after subsidence and adjustment of an instantaneously emplaced load, an initial structural height of 36 km yielded a final topographic height of ~23 km (welded contact) or of ~21 km (frictionless contact). This is similar to today's observed relief of 22 km relative to the surrounding plains [*Plescia*, 2004]. For a growing load scenario, the final topographic heights were only slightly different from those of the instantaneous load scenario.

There is much evidence for a high effective elastic thickness of the lithosphere T_e below Olympus Mons [*McGovern et al.*, 2004b; *Belleguic et al.*, 2005; *Beuthe et al.*, 2012]. Taking into account the loading history, *Beuthe et al.* [2012] found $T_e \geq 80$ km. *Belleguic et al.* [2005] reported a value of 93 ± 40 km. We chose a lithospheric thickness of $T_e = 90$ km. In contrast to the lithospheric thickness, the crustal thickness at Olympus Mons is poorly constrained by admittance analyses [*McGovern et al.*, 2004b; *Belleguic et al.*, 2005; *Beuthe et al.*, 2012], so we chose a value of 45 km following *Neumann et al.* [2004] and *Beuthe et al.* [2012].

3.2. Dynamic Setup

The parameters for the different parts of the model are summarized in Table 1. The densities are based on the results of admittance methods that evaluated gravity and topography data from the Mars Global Surveyor, Mars Express, and Mars Reconnaissance Orbiter missions. For Olympus Mons, under the assumption of no bottom loading (e.g., by a mantle plume beneath the volcano), *Beuthe et al.* [2012] modeled load densities of 3000–3100 kg m^{-3}, and for the volcano upper top load *Beuthe et al.* [2012] found a high density of $\geq$3150 kg m^{-3}. A density of $\rho = 3100$ kg m^{-3} was adopted here. For the crustal density, we chose $\rho = 2900$ kg m^{-3} in accordance with *Neumann et al.* [2004] and *Beuthe et al.* [2012].

Table 1. Olympus Mons Model Parameters

	Volcano	Crust	Lithospheric Mantle	Asthenospheric Mantle
Density ρ	3100 kg m^{-3}	2900 kg m^{-3}	3500 kg m^{-3}	3500 kg m^{-3}
Young's modulus E	40 GPa	40 GPa	120 GPa	120 GPa
Poisson's ratio ν	0.3	0.3	0.3	0.5
Viscosity η	-	-	-	1×10^{21} Pa s
Friction angle ϕ	40°	40°	40°	-
Dilation angle δ	10°	10°	10°	-
Cohesion c	6-66 MPa	66 MPa	66 MPa	-

The elastoplastic material properties of the volcanic cone used in this study were those for a basaltic rock mass with a Young's modulus of $E = 40$ GPa and a Poisson's ratio of $\nu = 0.3$ [cf. *Schultz*, 1995]. Postfailure behavior was included in the form of perfect plasticity. The failure envelope was described by a Mohr-Coulomb yield surface given by an internal friction angle and a cohesion. As the peak friction angles for natural joint surfaces in basalt vary between 33° and 46° [*Schultz*, 1995], $\phi = 40°$ was taken as a representative value. The dilation angle is 25% of the friction angle [*Hoek and Brown*, 1998]; hence, a value of the dilation angle of $\delta = 10°$ was selected. The elastoplastic parameters for the lithosphere were set to the same as the volcano elastoplastic parameters. For the volcanic edifice itself, a cohesion value of $c = 66$ MPa, appropriate for intact basalt, was used, but a value of $c = 6$ MPa, which is appropriate for a fractured or weathered basaltic rock mass [*Schultz*, 1995], was tested in addition.

The asthenospheric mantle was modeled as an incompressible, viscoelastic material [*Wu*, 1992; *Lund*, 2005] with initial elastic behavior followed by viscous relaxation. The Young's modulus of the lithospheric and asthenospheric mantle was assumed to be 3 times the crustal value [*McGovern and Solomon*, 1993]; hence, $E = 120$ GPa. The viscosity is temperature dependent and also influenced by a wet or dry mantle rheology (i.e., by the presence or absence of water), so that a reference viscosity of $\eta = 1 \times 10^{21}$ Pa s was adopted [*Karato and Wu*, 1993; *Breuer and Spohn*, 2006]. The Maxwell relaxation time of the asthenospheric mantle τ was then calculated from the Young's modulus and viscosity to be $\tau = 3\eta/E \approx 2.5 \times 10^{10} s \approx 800$ years. Greater or lower viscosity values would change the mantle Maxwell relaxation time proportionally and thus would affect the time until isostatic equilibrium is reached (see section 3.4). The asthenospheric mantle was assigned a density of $\rho = 3500$ kg m^{-3} following *Belleguic et al.* [2005] and *Beuthe et al.* [2012].

3.3. Boundary Conditions and Initial Conditions

The left and right boundaries of the axisymmetric model were fixed in the radial (r) direction but were free to move in the vertical (z) direction. The lower model boundary was fixed in the z direction (Figure 3). The crust and mantle components of the model were coupled through a welded contact. The contact between the volcano and the crust was either welded (completely coupled) or alternatively modeled as a frictional interface with a coefficient of basal friction μ of between 0.0 and 0.6 (i.e., completely to partly decoupled). Gravity was the only load applied to the model, with a gravitational acceleration of $g = 3.7$ m s^{-2} for Mars.

The initial state of stress in the lithosphere and asthenospheric mantle resulted from a geostatic stress field procedure in ABAQUS. This procedure led to a Poisson prestress in the lithosphere and to an isotropic prestress in the asthenospheric mantle. In a Poisson stress state, two principal stresses (the horizontal stresses) are equal but smaller compared to the third principal stress (the vertical stress), because of the compressibility of the material [*Turcotte and Schubert*, 2002]. In an isotropic stress state (lithostatic stress), all principal stresses are equal and correspond to the vertical stress $\rho g z$ [*Turcotte and Schubert*, 2002]. In our case, the latter applies to the asthenospheric mantle which we modeled as incompressible. Gravity loading in the volcano elements was not active at the beginning, in order to simulate an undisturbed basement upon which the volcano was constructed. Since buoyancy forces are not included in an ABAQUS static stress/displacement analysis, we used Winkler restoring forces, which are implemented in ABAQUS as elastic foundations, to account for isostatic compensation. These Winkler forces were applied to every density interface in the model [*Williams and Richardson*, 1991; *Wu*, 2004; *Lund*, 2005].

The implementation of Maxwell viscoelasticity and Winkler forces in ABAQUS was tested against the analytic model of *Pullan and Lambeck* [1981] for an elastic plate overlying a viscoelastic half-space in axisymmetry and loaded by two superimposed discs. The ABAQUS deflections were at maximum 5% higher compared with the analytic deflections, and the ABAQUS maximum differences of radial and hoop stresses were up to 7% lower compared with the analytic stress differences [see *Musiol*, 2013, Figure 4.11].

3.4. Temporal and Spatial Resolution

The model was subdivided into a sequence of analysis steps. To establish an equilibrium of applied loads and boundary conditions, a geostatic step was carried out initially, whereby gravity was applied to the crust and mantle only. In a second static step, gravity was turned on in the volcano elements. Since static steps do not account for time-dependent material properties, the response of the asthenospheric mantle during these two static steps is a function of its elastic properties.

Viscoelastic relaxation of the asthenospheric mantle was considered in a third, quasi-static (transient) step of 1 Ma duration. After about 460,000 years, changes in vertical displacement were negligible and are interpreted as corresponding to a state of isostatic equilibrium of the asthenospheric mantle and the volcanic load. The duration of this third analysis step was adapted according to the viscosity value, since the state of isostatic equilibrium was attained earlier for lower mantle viscosity and later for higher mantle viscosity by a factor proportional to the changed viscosity. For the instantaneous load scenario, the complete cone was emplaced instantaneously, which necessitates a growth time for the volcano much shorter than the mantle Maxwell relaxation time (about 800 years for the selected parameters).

Since such a short growth time is unlikely for Olympus Mons (see section 2), we also modeled a growth time for the volcano longer than the mantle Maxwell relaxation time (growing load scenario). Longer growth times were modeled with load increments, to allow for viscoelastic relaxation of the asthenospheric mantle between the analysis steps. The volcano was arbitrarily divided into five units of equal volume such that the growing cone had the following radius/height dimensions: 175/21 km, 220/26 km, 252/30 km, 277/33 km, and 300/36 km (Figure 3, box at top right). The entire volcano was meshed from the beginning, but gravity loading was not active in the volcano elements at that time. Hence, there was no initial deformation of lithosphere and asthenospheric mantle due to the volcano in the first geostatic analysis step. All volcano elements were then removed in a second static step. Volcano growth was simulated by successive reactivation of the volcano mesh elements of each unit in static steps. Once reactivated, the mesh elements of a certain volcano unit were loaded with gravity, and the response of the asthenospheric mantle to the active load was analyzed in a quasi-static step of 1 Ma duration. The total analysis time for the growing load scenario was therefore 5 Ma. The emplacement of five units in, e.g., 50 or 500 Ma would not influence the results, since load, crust, and mantle had attained isostatic equilibrium within 460,000 years of the emplacement of each unit.

The volcanic edifice and crust had an irregular mesh of quadratic and triangular elements (Figure 4). The minimum element size in the volcanic cone was 0.3 km. The element size in the volcanic cone increased up to 1 km at the volcano-crust interface. In the crust, the minimum element size was 0.5 km, and the maximum element size was 5 km. The mantle was assigned a structured mesh of quadratic elements with an element size of 10 km.

3.5. Model Limitations

Since the gravity-driven deformation of the volcano-crust-mantle system is the main interest of this work, intrusive and extrusive volcanic activity was not taken into account. In addition, the influences of temperature, and pore fluids were not considered, although we are aware of the fact that the presence of pore water can alter the faulting process and promote sliding along fault planes due to the effective stress principle and hydrothermal weakening [*Hubbert and Rubey*, 1959; *Day*, 1996]. The effect of pore-fluid pressure was implicitly considered for the volcano base, however, by varying the friction coefficient there. The lithosphere underlying Olympus Mons was approximated as a flat plate, because the effect of planetary curvature is negligible for the selected combination of lithospheric thickness and load width [*Turcotte et al.*, 1981; *Cailleau et al.*, 2005].

The two-dimensional axisymmetric model is a simplified geometry of Olympus Mons, which is characterized by asymmetries arising from an underlying regional slope [e.g., *Plescia*, 2004; *McGovern and Morgan*, 2009]. An improved model could include three dimensions to incorporate the real topography. A fully 3-D model could
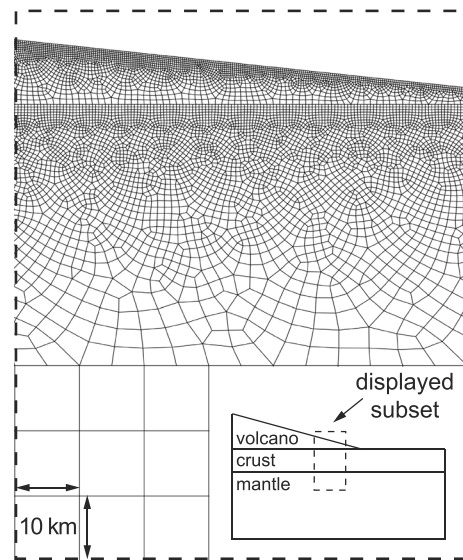
Figure 4. A portion of the model mesh, showing mesh detail.

also overcome another limitation of the axisymmetric approach, which is that predicted faults are constrained to lie within or perpendicular to the radial plane of cross section. As discussed below, the possibility that in reality faults may strike at orientations between radial and concentric must be considered when comparing the model results to nature. However, we do not think that this factor affects substantially the main results of this study.

4. Results

Altogether, eight models were evaluated in which the development of lithospheric flexure, of plastic straining in the crust and in the volcano, and of principal stresses near the surface were investigated. Since the asthenospheric mantle was viscoelastic, the development of these variables was time dependent.

For the instantaneous load scenario, a welded contact between volcano and crust (completely coupled) was considered in model 1. In models 2 to 5, the coefficient of friction μ at the volcano-crust interface was progressively changed from 0.6 (frictional contact, partly decoupled) to 0.0 (frictionless contact, completely decoupled). For the growing load scenario, the contact at the volcano-crust interface was either welded (model 6) or was frictionless (model 8). The effect of a lower cohesion value of 6 MPa was tested for a growing volcano with a welded contact (model 7).

4.1. Flexure- and Spreading-Related Movements

As already noted in section 3, a trade-off between the effective elastic thickness of the lithosphere and the initial structural volcano height controls the final topographic volcano height. Hence, a given topographic height can be reproduced either with a thin lithosphere and a tall volcano, which leads to substantial lithospheric flexure and a deep volcanic root, or with a thick lithosphere and a smaller volcano that leads to minor lithospheric flexure and a shallow volcanic root. The volcanic root in this case is that subsurface portion of the volcano that has been above ground level prior to flexure. In the end-member case when the volcano height becomes negligible compared to the lithospheric thickness, the initial structural volcano height is about the final topographic volcano height.

Maximum downward flexure of the surface of the elastic lithosphere for the instantaneous load scenario was −12.9 km in model 1 (welded contact) and −14.7 km in model 5 (frictionless contact). The maximum upward flexure of the surface of the elastic lithosphere (bulge) had an amplitude of about 180 m and was situated at a radial distance of 743 km (model 1) and 718 km (model 5) from the volcano center. Maximum downward flexure for the growing load scenario was −13.4 km in model 6 (welded contact) and −14.9 km in model 8 (frictionless contact). The differences in flexure can be attributed to stiffening effects for the welded contact [*McGovern and Solomon*, 1993]: welding the volcano to the lithosphere effectively thickens the latter, hence reducing flexure for a given load. Our results predict a volcanic root reaching down to ∼14 km below the topographic base of Olympus Mons. This root constitutes about 40% of the total structural height of 36 km, which compares well with the case of Hawaii on Earth, where geophysical data show an ∼8 km deep root lying below the topographic height of ∼9 km; i.e., Hawaii's total structural height is ∼17 km [*Zucca et al.*, 1982].

With sustained flexure, the volcano-crust interface can become a detachment for $\mu = 0.0 – 0.6$. For all but the welded cases the volcano spreads (i.e., thrusted) outward over the crust. However, in the instantaneous load scenario and even for the frictionless contact, the accumulated relative tangential motion at the volcano-crust interface was only 2.3 km at the end of mantle relaxation. This corresponds to an increase in model volcano radius of <1%. For the growing load scenario and for $\mu = 0.0$, relative tangential motion along the volcano-crust interface was even lower: 0.14 km at the end of mantle relaxation.
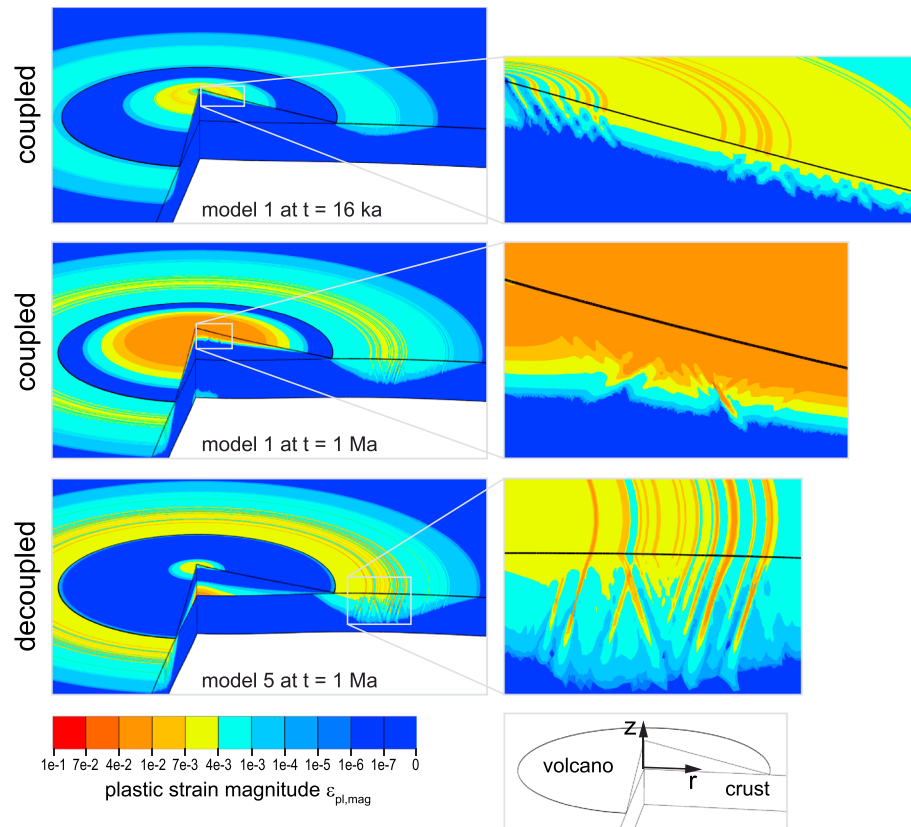
Figure 5. Predicted zones of plastic strain concentrations for edifice-induced lithospheric flexure in the instantaneous load scenario. Block diagrams of volcano and crust with twofold exaggerated z coordinate. Close-ups of model 1 (cohesion 66 MPa, welded contact) show concentric faults in the volcano dipping inward and outward 16,000 years and 1 million years after load emplacement. Close-up of model 5 (cohesion 66 MPa, frictionless contact) shows concentric faults in the crust dipping inward and outward 1 million years after load emplacement.

4.2. Strain Evolution

The results were plotted as accumulated plastic strain magnitude $\epsilon_{pl,mag}$, given as

$$\epsilon_{pl,mag} = \sqrt{\frac{2}{3}\epsilon_{pl} : \epsilon_{pl}},$$

where the colon denotes a scalar product and ϵ_{pl} is the plastic strain matrix. The results exhibit three regions of plastic straining: On the volcano flanks, in the crust around the volcano, and within the volcano at or just above the volcano-crust interface. We refer to zones of high plastic strain as faults. The depth of faults can only be estimated from the model depth of significant plastic straining, which depends in part on the threshold value we chose for the plastic strain magnitude. Note that faults in nature are fractures, but plastic straining is a step prior to fracturing. To visualize individual faults, block diagrams of volcano and crust were created by revolving the cross-sectional strains around a vertical axis (Figures 5 and 6).

4.2.1. On the Volcano Flanks

Plastic strain on the volcano flanks was promoted by instantaneous loading and by low cohesion. It was inhibited by incremental loading and by reducing the basal friction coefficient. For an instantaneously emplaced volcano that was welded to the crust (model 1), concentric faults appeared on the upper volcano flanks 16,000 years after load emplacement (Figure 5). These faults dipped inward or outward, and the zone of plastic straining in which they develop migrated down the volcano flanks with time. At the end of mantle relaxation, after 1 Ma, these faults had grown deeper, with individual large faults dominating over numerous small faults (Figure 5; see also Movie S1 in the supporting information). As the friction coefficient at the volcano base was progressively reduced, the areal extent of plastic strain on the flanks was also reduced. For the decoupled end-member case (model 5), only the area around the summit underwent plastic strain (for high strength).
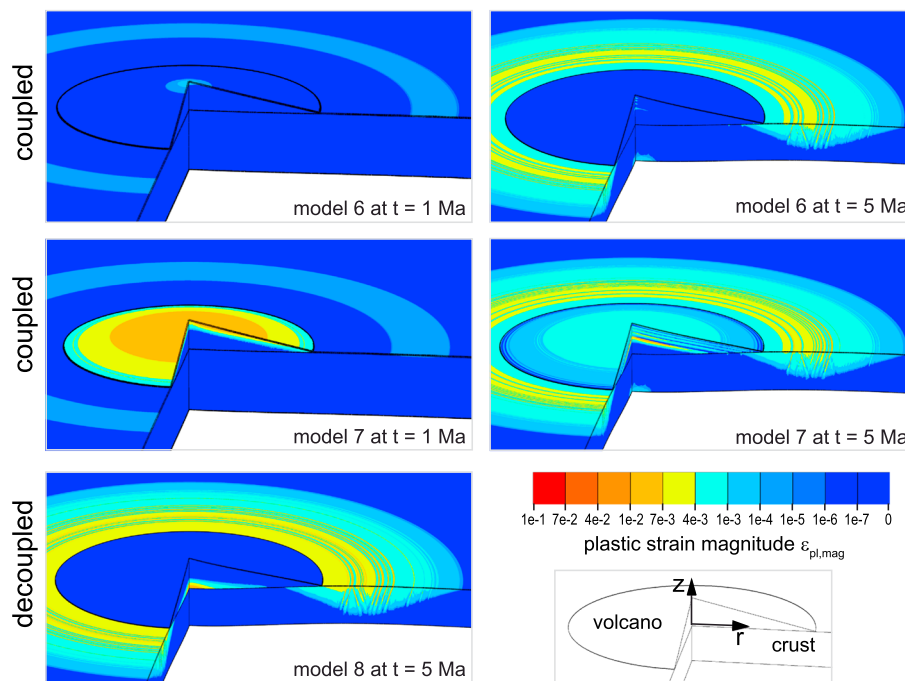
Figure 6. Predicted zones of plastic strain concentrations for edifice-induced lithospheric flexure in the growing load scenario. Block diagrams of volcano and crust with twofold exaggerated z coordinate. Model 6 (cohesion 66 MPa, welded contact) did not develop plastic strain at the volcano surface, whereas model 7 (cohesion 6 MPa, welded contact) did. Model 8 (cohesion 66 MPa, frictionless contact), developed plastic strain at the volcano-crust interface.

For the incrementally grown volcano welded to the crust and with a cohesion of 66 MPa, little plastic straining of the volcano flanks occurred after emplacement of the first volcano unit, and none occurred after emplacement of the fifth volcano unit (model 6 in Figure 6). In contrast, plastic straining affected the complete surface of the first volcano unit and was manifest on every incrementally added volcano unit with a cohesion of 6 MPa (model 7 in Figure 6; see also Movie S2 in the supporting information).

4.2.2. In the Volcano Above the Volcano-Crust Interface

Plastic strain was observed at or just above the volcano-crust interface for only very low basal friction coefficients ($\mu \leq 0.1$). For the instantaneous load scenario with a frictionless contact between volcano and crust (model 5), plastic deformation at the volcano-crust interface started 4700 years after load emplacement, whereas for $\mu = 0.1$ (model 4) plastic deformation started only 47,000 years after load emplacement. For the growing load scenario and frictionless contact between volcano and crust (model 8), plastic deformation at the volcano-crust interface began 35,000 years after emplacement of the first volcano unit. At the end of mantle relaxation, plastic deformation affected the entire volcano-crust interface for the instantaneously emplaced volcano but only half of the volcano-crust interface for the growing volcano (Figures 5 and 6).

4.2.3. In the Crust Around the Volcano

At the end of mantle relaxation, concentric faults that dipped inward and outward were visible down to depths of 20 km in the crust around the volcano for all models (Figures 5 and 6). Faults in the crust appeared 8500 years after setup of the instantaneously emplaced volcano in model 1 and 82,000 years after setup of the first unit of the incrementally grown volcano in model 7. The magnitude of plastic strain in the crust was smallest for the welded contact (model 1) and largest for the frictionless contact (model 5). Again, this can be attributed to an increase of the effective elastic thickness (i.e., stiffening) of the lithosphere by the welded volcano, as already reported by *McGovern and Solomon* [1993].

4.3. Combined Stress/Strain Evolution

Fault orientation and slip sense are governed by the principal stress orientation. Due to axisymmetry and the projection method, Figures 5 and 6 are restricted to showing only concentric faults. However, stresses in the models were quasi three-dimensional, and radial/oblique structures are observed. Thus, and notwithstanding the remaining limitations of the 2-D axisymmetry, we use Andersonian fault theory to improve the prediction of the fault type and orientation. After *Anderson* [1951], thrust faulting results from vertical
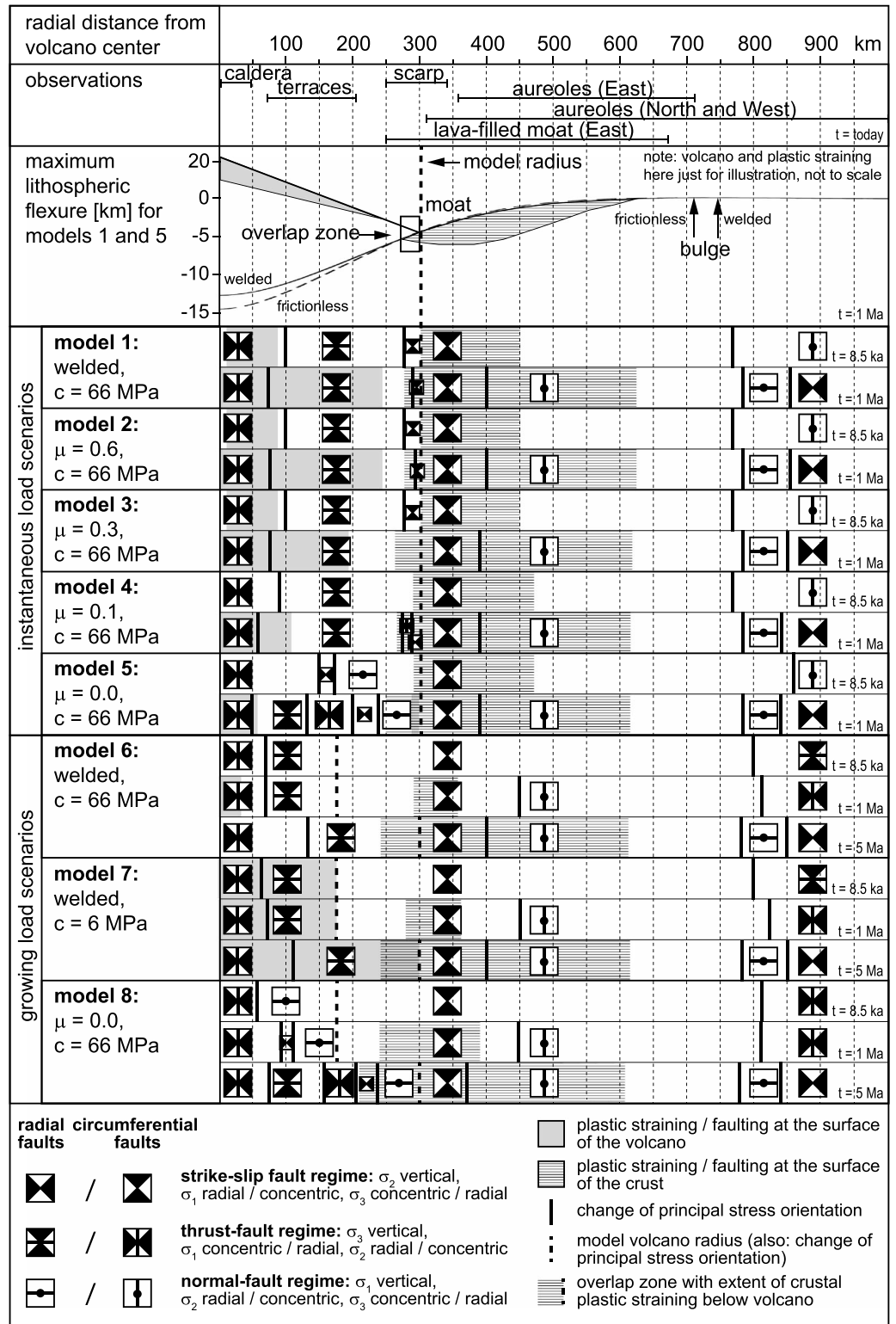
Figure 7. Time-dependent surface principal stress orientations and fault formation in comparison to observations. The fault symbols also represent principal stress directions in plan view: the black hourglass symbol denotes the direction of maximum compressive stress (σ_1), and the bar denotes the direction of intermediate compressive stress (σ_2). The results were analyzed at three different times: at the beginning of plastic deformation at 8500 years, at the end of mantle relaxation for the instantaneously emplaced volcano at 1Ma, and at the end of mantle relaxation for the incrementally grown volcano at 5 Ma. The contact between volcano and crust was either welded or modeled as a frictional interface defined by a coefficient of basal friction μ. The cohesion of the volcanic edifice is denoted by c.

minimum compression (σ_3), normal faulting from vertical maximum compression (σ_1), and strike-slip faulting from vertical intermediate compression (σ_2). The remaining principal stresses are oriented horizontal to the surface in each case.

The results for the instantaneous load scenarios were evaluated at the beginning of plastic deformation after 8500 years and at the end of mantle relaxation after 17 Ma. For the growing load scenarios, results were analyzed both at 8500 years and 1 Ma after emplacement of the first volcano unit and at 5 Ma at the end of mantle relaxation after the emplacement of the fifth volcano unit (Figure 7).

4.3.1. On the Volcano Flanks

Regardless of the properties of the volcano-crust interface, of the cohesion of the volcanic edifice or of the loading history, the summit area of all models was characterized by radial maximum compression and vertical minimum compression (Figure 7). In the case of plastic straining, this yielded concentric thrust faults, as illustrated by Figure 5.

The middle to lower volcano flanks were characterized by a zone of hoop maximum compression and vertical minimum compression in the coupled models 1–4, 6, and 7. Radial thrust faults would therefore likely form there. In addition, a narrow zone at the cone toe moved into the strike-slip fault regime. The orientation of strike-slip faults differed for differing values of basal friction, however. At high friction ($\mu \geq 0.3$), the strike-slip faults were likely to be near concentric. At lower basal friction ($\mu = 0.1$, model 4), the strike-slip faults in the toe region were predicted to be near radial.

The stress state in the middle to lower volcano flanks of the completely decoupled models 5 and 8 ($\mu < 0.1$) was remarkably different from all other models and changed substantially with time as strain accumulated. Early in the deformational process, the middle to lower flanks were characterized by hoop minimum compression and vertical maximum compression, so in the case of faulting we would expect radial normal faults. Later in the deformational process, the stress state in the middle flanks changed to one in which radial and/or concentric thrust faults would form. The stress state in the lower flanks altered with time to favor development of near-radial strike-slip faults as well as radial normal faults.

The occurrence of plastic straining and faulting depends strongly on the cohesion, as evident from a comparison of models 6 and 7. Moreover, the stress states and their distribution in these models are the same regardless of the cohesion (Figure 7). Only the magnitude (and extent) of the plastic strain differs. Hence, from model 8, we can infer the result of a model in which a low cohesion edifice with a frictionless basal contact was grown incrementally. Such a hypothetical model, which should be investigated in future work, would have a stress pattern identical to that in model 8 (Figure 7) and differ only in having significant plastic strain from summit to toe.

4.3.2. In the Volcano Above the Volcano-Crust Interface

Only surface stresses were analyzed in Figure 7, representing the fault zones on the volcano flanks and in the crust around the volcano. For models 4, 5, and 8, i.e., with low or no basal friction, there was an additional zone of faulting above the volcano-crust interface (Figures 5 and 6). Analysis of the stress state in this zone shows vertical maximum compression and hoop minimum compression, which would favor radial normal faulting.

4.3.3. In the Crust Around the Volcano

In the proximal flexural moat of all models (1 to 8), plastic deformation began in a zone of hoop maximum compression and radial minimum compression (Figure 7). This stress state would lead to near-concentric strike-slip faulting initially. With low confining pressure, such as expected near the surface, the same stress state could also lead to vertical jointing [*Schultz and Zuber*, 1994]. With ongoing plastic deformation, however, the zone of predicted strike-slip faulting narrowed markedly and was ultimately restricted to an area immediately outside the toe of the volcano. The maximum compression in the distal flexural moat extending to the bulge rotated to vertical, while the minimum compression remained radial. This rotation resulted in concentric normal faulting in most of the area that would have been predicted to fail by strike-slip faulting or vertical jointing under purely elastic model conditions. This result is of relevance for the so-called "strike-slip paradox" [e.g., *McGovern and Solomon*, 1993; *Schultz and Zuber*, 1994; *Freed et al.*, 2001]. We will come back to that later in section 5.

The zone of crustal deformation around the volcano also extended under the volcano's toe, such that in plan view this deformation zone overlapped with that on the volcano's lowermost flanks (Figure 7). The size of this "overlap zone" increased with decreased basal friction coefficient and incremental growth.

The stress field beyond the bulge existed in the normal fault regime and, with further distance from the bulge, in the strike-slip fault regime for all models at the end of mantle relaxation, but in all cases stresses were insufficient to form faults in this area for the strengths modeled here.

5. Discussion

In this study, we simulated the deformation of the largest known shield volcano by using finite element models that included a variable basal detachment and an elastoplastic rheology, to account for the combined effects of lithospheric flexure and volcanic spreading. We tested eight different model configurations, in which we varied the time of loading (instantaneous versus growing load scenario), the friction coefficient between volcano and crust (completely coupled versus completely to partly decoupled), and the cohesion of the volcano (66 MPa versus 6 MPa). This is the first study in which this combination of processes and rheological behavior has been implemented with numerical methods.

In this section, we first discuss our model results with respect to the morphotectonic features of our case study, Olympus Mons. We then consider the wider implications of our results for other volcanoes on Mars and for our understanding of gravity-driven volcano deformation in general. These more general implications concern the so-called strike-slip paradox of volcano-induced lithospheric flexure, the roles of plasticity and cohesion in gravity-driven deformation of volcanoes, the role of basal friction in the interaction of flexure and spreading, and the possible impacts of these deformations on a large volcano's susceptibility to flank collapse.

5.1. The Morphotectonic Features of Olympus Mons: A Product of Low Basal Friction Combined With Low Edifice Cohesion

Our models illustrate the importance of incorporating a realistic rock mass strength in the prediction of deformation at volcanoes. For instance, the growing load scenarios with a cohesion of 66 MPa in the volcano (Figure 6, models 6, and 8) did not produce any faults on the model volcano flanks at the end of deformation, whereas a growing load with sufficiently low cohesion of, e.g., 6 MPa or lower did so (Figure 6, model 7). In interpreting the model results and comparing them with structures observed in nature, one must therefore examine not only the plastic strain patterns in the models but also the stress patterns in areas that have not failed. This is because areas that do not undergo failure in the model could do so in reality if the cohesion in nature were lower than that modeled here. In addition, the emplacement of a major portion of the edifice of Olympus Mons in a geologically short time, in order to induce stresses large enough to fail high-cohesion flanks [*McGovern and Solomon*, 1993], may not be needed if an edifice cohesion is on the order of a few MPa, as is common in nature [*Schultz*, 1995].

Observations of terraces, scarp, and aureoles (see section 2 and Figure 2) were plotted as a function of radial distance in Figure 7, for comparison with our numerical results. Terraces on the flanks of Olympus Mons cover one third to two thirds the radial distance from summit to scarp. This spatial extent of terracing is consistent with predictions of a region of plastic strain and thrust faulting on the model volcano flanks at the end of mantle relaxation. An exception is the summit caldera complex and a 10–60 km wide zone immediately around it, where although consistently predicted there by our numerical models, terraces are apparently absent. This can be attributed to overprinting of terraces in the vicinity of the summit region of Olympus Mons by caldera-related deformation and magmatism, which was not accounted for in our models. A thrust-fault regime covering up to two thirds, or more, of the way down the flank was explicitly produced for instantaneous loading with high basal friction conditions ($\mu \geq 0.3$) and for incremental loading with welded basal friction conditions and a volcano cohesion of 6 MPa. However, even for those models with low to zero basal friction and with plastic deformation inhibited for a cohesion value of 66 MPa the stress state was consistent with thrust faulting along two thirds of the flank or more (Figure 7). Intriguingly, the models with a basal friction coefficient of zero (models 5 and 8) showed a clear transition from thrust faulting to strike-slip and normal faulting at about two thirds the way down the flank—as observed at Olympus Mons.

An apparent discrepancy between the model results and the observations of Olympus Mons is that most terraces on the flanks of Olympus Mons appear to follow a concentric pattern, whereas the models predicted mainly radial thrust faults on the edifice flanks. A close inspection of Figure 2 reveals that the boundaries of the terraces are rather linear, however, and that most trend obliquely with a deviation from the concentric orientation by 45° in places. Therefore, a more nuanced and complex interpretation of terraces with respect

to the two-dimensional models is needed for several reasons. First, for the two-dimensional axisymmetric models, and in turn the Andersonian faulting theory used to interpret them, the principal stresses are fixed to be radial or concentric. This leads to an either/or prediction of radial or concentric thrust faulting. If the difference in magnitude between the maximum and intermediate principal stresses is small, however, such a distinction is not necessarily very meaningful since such conditions could lead to faults of both orientations in reality. Interestingly, the models with a completely decoupled volcano ($\mu = 0.0$) showed such a small difference in the principal stress magnitudes, resulting in alternating zones of stresses with concentric and radial thrust patterns along the volcano flanks (see Figure 7). Second, it could be simply that in nature, the principal stresses are oblique, leading to obliquely oriented thrusts. Third, even with radial and concentric principal stresses, obliquely oriented thrusts could emerge from a truly three-dimensional strain field [*Krantz*, 1988], something that was not simulated here. Therefore, given the limitations of our models, we prefer not to overinterpret the predicted orientation of thrust faulting on the model flanks—most important is that thrusting was predicted.

The lower flanks of Olympus Mons feature radial scarps (Figure 2a). Only models with very low basal friction conditions ($\mu < 0.1$) produced a stress state allowing for near-radial strike-slip faults and radial normal faults on the lowermost flanks [cf. *McGovern and Solomon*, 1993]. With high cohesion, such faulting was predicted to occur only in a narrow zone at the cone toe for instantaneous loading. Nevertheless, as indicated by comparing models 7 and 8, we expect normal faulting on the lowermost flanks for the growing load model scenario, if a reduced cohesion value was used. Importantly, these faults could act as weaknesses along which sector collapses and landslides could develop [*McGovern and Solomon*, 1993; *van Wyk de Vries and Francis*, 1997]—see below.

In summary, our models indicate that lithospheric flexure in combination with a very low basal friction and a realistically low value for the volcanic rock mass strength can account for the structural arrangement on Olympus Mons. Lithospheric flexure has an overriding influence on the model results, as can be seen from the overall similar stress states for all models in Figure 7. Further, this process is responsible for the formation of flank terraces, as already argued by *McGovern and Solomon* [1993], *Byrne et al.* [2009], and *Byrne et al.* [2013]. The effect of volcanic spreading is mainly seen on the lowermost flanks of Olympus Mons and may account for observed radial scarps near the base of the volcano [cf. *McGovern and Solomon*, 1993]. A low-friction detachment plane enabling spreading and collapse of Olympus Mons' lower flanks may have developed from interstitial ice [*Tanaka*, 1985] or clay-rich and pore fluid overpressured Noachian sediments [*Hubbert and Rubey*, 1959; *McGovern et al.*, 2004a, 2014].

5.2. Observations Consistent With Gravity-Driven Deformation of Other Martian Volcanoes

If flank terraces act as an indicator for lithospheric flexure, this implies vice versa that the other Martian shield volcanoes that possess flank terraces, namely, Alba Patera, Albor Tholus, the three Tharsis Montes, Elysium Mons, Hecates Tholus, and Uranius Patera [*Byrne et al.*, 2009], have all downflexed the elastic lithosphere below them. Whereas *Byrne et al.* [2009] and *Byrne et al.* [2013] interpreted terrace-bounding faults as inwardly dipping thrusts, the dip of the terrace-bounding thrust faults in our models was inward as well as outward relative to the cone center.

Flexure of the lithosphere was already considered for Arsia Mons, Pavonis Mons, and Ascraeus Mons [*McGovern and Solomon*, 1993]; for Alba Patera; and for Elysium Mons [*Comer et al.*, 1985]. Since Elysium Mons and the smaller shields, Albor Tholus, and Hecates Tholus, are all part of the Elysium Volcanic Province, terraces observed on these three volcanoes could be attributed to downflexure of the elastic lithosphere below the entire Elysium rise. The Elysium rise and Alba Patera are both long-wavelength structures, so-called domal rises [*McGovern et al.*, 2002]. In the Tharsis Volcanic Province Uranius Patera is much smaller compared with the other terraced volcanoes. Possibly a major portion of this volcano was buried by lava flows.

Unlike Olympus Mons, other Martian volcanoes show faulting of the crust in their immediate vicinity and are thus suitable for comparison to the predictions of our models for this region (Figure 7). Concentric graben were documented on and around the Tharsis Montes [*Crumpler and Aubele*, 1978] and around Elysium Mons [*Comer et al.*, 1985]. Alba Patera is partly associated with concentric graben, which have also been influenced by the regional stress field of the Tharsis Volcanic Province [*Cailleau et al.*, 2003].

5.3. The Role of Nonelastic (Plastic) Deformation in Gravity-Driven Deformation of Large Volcanoes: A Solution to the Strike-Slip Paradox?

Elastic flexure models with axisymmetric surface loads [e.g., *Pullan and Lambeck*, 1981; *Comer et al.*, 1985] predict strike-slip faulting in the crust around the load. In contrast, only concentric graben, rather than strike-slip faults, are observed around large volcanoes. This is the so-called strike-slip paradox [*Freed et al.*, 2001].

One solution to this paradox is that the predicted failure mode in the region surrounding the load can change with time from initial circumferential normal faulting to later strike-slip faulting [*McGovern and Solomon*, 1993]. The argument here is that in reality, the earlier normal faulting would relieve most of the flexural stress, and therefore, concentric graben are observed around large volcanoes. *Schultz and Zuber* [1994], in turn, argued that a tensile failure criterion should be taken into account when evaluating stress results from elastic flexure models. They asserted that the stress state associated with strike-slip faulting is also consistent with vertical jointing, which could also appear as concentric troughs around large edifices. Finally, consideration of planetary curvature and more sophisticated faulting criteria, although not applied in this work, led to the prediction of only a narrow zone of strike-slip faulting around surface loads [*Freed et al.*, 2001].

Our models showed that with ongoing plastic deformation, the zone of stresses compatible with strike-slip faulting immediately around the load narrowed markedly as it moved toward the volcano. The strike-slip stress state was replaced by one compatible with circumferential normal faulting, at which point these areas were predicted to undergo failure (Figure 7). This provides an alternative explanation for the strike-slip paradox: the model rheology and method of failure prediction, specifically elastic versus plastic in this case.

5.4. Interaction of Lithospheric Flexure and Volcano-Spreading at Large Volcanoes: The Role of Basal Friction

The interaction of lithospheric flexure and volcanic spreading in concert has been previously investigated by both numerical [*McGovern and Solomon*, 1993] and analog [*Byrne et al.*, 2013] modeling techniques. McGovern and Solomon's axisymmetric finite element setup is similar to our setup. We have benefited from recent mission data to better constrain the modeling parameters, however, and we have included plasticity, a high spatial resolution to resolve discrete faults, and a basal detachment with variable friction. Our results showed that the effects of varying basal friction are remarkably small until very low friction coefficients are reached, meaning that spreading along such a frictional detachment may require very special circumstances, particularly high pore fluid pressures, to occur.

Analog models of hybrid sagging-spreading with a viscous (rather than frictional) basal detachment produced thrust faults on the cone's upper flanks, normal faults on the lower flanks and in the surroundings of the cone, and a fold-and-thrust belt developed around the cone's base [*Byrne et al.*, 2013]. This structural arrangement is similar to the results of our model of an instantaneously emplaced volcano decoupled from the crust (model 5 in Figure 7), aside from the formation of a fold-and-thrust belt. Thus, our model results provide additional supporting evidence for a hybrid sagging-spreading architecture of Olympus Mons. In addition, they indicate that the structural architecture is similar whether lithospheric flexure interacts with spreading caused by frictional or viscous basal rheologies.

The role of magma and magmatic intrusion is a factor not yet considered here or in previous models of the interaction of lithospheric flexure and spreading. Terrestrial volcanoes such as Mount Etna (Sicily), Kilauea (Hawaii), and Piton de la Fournaise (La Réunion) are known to grow by intruding dike complexes along rift zones [*Le Corvec and Walter*, 2009; *Le Corvec et al.*, 2014]. This magma forcing can affect the degree of volcanic spreading and horizontal flank displacement and may promote or hinder associated fault activity [*Le Corvec et al.*, 2014]. Scaled analog models produced flank-parallel listric normal faults as typical spreading structures and graben as typical rift zone intrusion structures on the shield [*Le Corvec and Walter*, 2009]. Flank-parallel graben and troughs on the lower flanks of Olympus Mons (Figure 2a) are likely landslide related, and *Bleacher et al.* [2007] argued that on the basis of an apparent lack of eruptive centers on the north and south flank, Olympus Mons has not developed rift zones. Nonetheless, future studies of the interaction of the three processes lithospheric flexure, spreading, and intrusions would be fruitful for our understanding of large volcanoes in general.

5.5. Implications for Volcano Collapse

An important additional finding of this study is that partial collapse of a volcano that is subject to considerable basement or lithospheric flexure is more likely to occur farther from the volcano center, whereas in models of

pure spreading, the volcanic edifice undergoes extensional deformation throughout [*Merle and Borgia*, 1996; *Oehler et al.*, 2005; *Delcamp et al.*, 2008]. The volcano center is stabilized by flexure due to inward tilting that leads to compression of the upper flanks, even in the case of a completely decoupled cone. The basal scarp of Olympus Mons is located a substantial distance from the volcano center, similar to the case of Hawaii on Earth, and both are subject to lithospheric flexure. This configuration is in contrast to smaller terrestrial volcanoes such as Socompa in Chile [*van Wyk de Vries et al.*, 2001], or Mombacho and Maderas in Nicaragua [*Borgia et al.*, 2000], which are not capable of flexing the basement significantly, and hence lack compression of the upper flanks. At those volcanoes, spreading, landsliding, and flank collapse have altered the edifices severely up to their summits, and so without flexure and flank compression, a collapse may be more likely to intersect the volcano plumbing system and so to give rise to coeval eruption, as at Mount St. Helens, for example. The stabilizing effect that lithospheric flexure has on the central portion of a volcano implies that the degree to which a volcano can undergo collapse depends on the relation between volcano size and lithospheric thickness [cf. *Byrne et al.*, 2013]

Nonetheless, observations of Olympus Mons and the result of our models indicate that collapse of a flexing volcano is possible with a very low basal friction. Moreover, the long runout distances of the aureole deposits associated with the circumferential scarp could result from lubrication by abundant water at the base of Olympus Mons [*De Blasio*, 2011]. Future work should therefore focus on the role of water, ice, and sediments for volcanic spreading and collapse.

6. Conclusions

Observations of upper flank terraces and a lower flank circumferential scarp point to gravity-driven deformation early in the evolution of Olympus Mons on Mars. Elastoplastic finite element modeling supports earlier interpretations of terraces on the volcano's upper flanks as bounded by thrust faults resulting from lithospheric flexure. The presence and expression of flank terraces depend on the coupling of volcano and crust, on the time of volcano growth relative to mantle relaxation, and on the edifice cohesion. In models with an edifice cohesion of 66 MPa, appropriate for intact basalt, a growth time of the volcano that is short compared with the mantle Maxwell relaxation time (modeled as an instantaneous load scenario) is a requirement to produce surface faults on the shield. However, the formation of faults on the shield can also be achieved in models with a prolonged volcano growth (modeled as a growing load scenario) with edifice cohesions ≤6 MPa, corresponding to a fractured or altered basaltic rock mass. Although lithospheric flexure may promote compression and thus stability of the edifice, the presence of a very low friction detachment at the edifice base can lead to extension and formation of radial normal faults on the lowermost flanks. These faults may weaken the lowermost flanks and make them susceptible to collapse.

References

Anderson, E. M. (1951), *The Dynamics of Faulting*, 2nd ed., Oliver and Boyd, Edinburgh.

Basilevsky, A. T., et al. (2005), Morphology and geological structure of the western part of the Olympus Mons volcano on Mars from the analysis of the Mars Express HRSC imagery, *Sol. Syst. Res.*, *39*, 85–101, doi:10.1007/s11208-005-0025-2.

Basilevsky, A. T., S. C. Werner, G. Neukum, J. W. Head, S. van Gasselt, K. Gwinner, and B. A. Ivanov (2006), Geologically recent tectonic, volcanic and fluvial activity on the eastern flank of the Olympus Mons volcano, Mars, *Geophys. Res. Lett.*, *33*, 85–101, doi:10.1029/2006GL026396.

Belleguic, V., P. Lognonné, and M. Wieczorek (2005), Constraints on the Martian lithosphere from gravity and topography data, *J. Geophys. Res.*, *110*, E11005, doi:10.1029/2005JE002437.

Beuthe, M., S. Le Maistre, P. Rosenblatt, M. Pätzold, and V. Dehant (2012), Density and lithospheric thickness of the Tharsis Province from MEX MaRS and MRO gravity data, *J. Geophys. Res.*, *117*, E04002, doi:10.1029/2011JE003976.

Bleacher, J. E., R. Greeley, D. A. Williams, S. C. Werner, E. Hauber, and G. Neukum (2007), Olympus Mons, Mars: Inferred changes in late Amazonian aged effusive activity from lava flow mapping of Mars Express High Resolution Stereo Camera data, *J. Geophys. Res.*, *112*, E04003, doi:10.1029/2006JE002826.

Borgia, A., J. Burr, W. Montero, L. D. Morales, and G. E. Alvarado (1990), Fault propagation folds induced by gravitational failure and slumping of the Central Costa Rica volcanic range—Implications for large terrestrial and Martian volcanic edifices, *J. Geophys. Res.*, *95*, 14,357–14,382, doi:10.1029/JB095iB09p14357.

Borgia, A., P. T. Delaney, and R. P. Denlinger (2000), Spreading volcanoes, *Annu. Rev. Earth Planet. Sci.*, *28*, 539–570.

Breuer, D., and T. Spohn (2006), Viscosity of the Martian mantle and its initial temperature: Constraints from crust formation history and the evolution of the magnetic field, *Planet. Space Sci.*, *54*(2), 153–169, doi:10.1016/j.pss.2005.08.008.

Byrne, P. K., B. van Wyk de Vries, J. B. Murray, and V. R. Troll (2009), The geometry of volcano flank terraces on Mars, *Earth Planet. Sci. Lett.*, *281*, 1–13, doi:10.1016/j.epsl.2009.01.043.

Byrne, P. K., E. P. Holohan, M. Kervyn, B. van Wyk de Vries, V. R. Troll, and J. B. Murray (2013), A sagging-spreading continuum of large volcano structure, *Geology*, *41*(3), 339–342, doi:10.1130/G33990.1.

Cailleau, B., T. R. Walter, P. Janle, and E. Hauber (2003), Modeling volcanic deformation in a regional stress field: Implications for the formation of graben structures on Alba Patera, Mars, *J. Geophys. Res.*, *108*(E12), 5141, doi:10.1029/2003JE002135.

Cailleau, B., T. R. Walter, P. Janle, and E. Hauber (2005), Unveiling the origin of radial grabens on Alba Patera volcano by finite element modelling, *Icarus*, *176*, 44–56, doi:10.1016/j.icarus.2005.01.017.

Carr, M. H., R. Greeley, K. R. Blasius, J. E. Guest, and J. B. Murray (1977), Some Martian volcanic features as viewed from the Viking orbiters, *J. Geophys. Res.*, *82*(28), 3985–4015, doi:10.1029/JS082i028p03985.

Comer, R. P., S. C. Solomon, and J. W. Head (1985), Thickness of the lithosphere from the tectonic response to volcanic loads, *Rev. Geophys.*, *23*, 61–92.

Crumpler, L. S., and J. C. Aubele (1978), Structural evolution of Arsia Mons, Pavonis Mons, and Ascreus Mons: Tharsis region of Mars, *Icarus*, *34*, 496–511, doi:10.1016/0019-1035(78)90041-6.

Day, S. J. (1996), Hydrothermal pore fluid pressure and the stability of porous, permeable volcanoes, in *Volcano Instability on the Earth and Other Planets*, edited by W. J. McGuire, A. P. Jones, and J. Neuberg, pp. 77–93, *Geol. Soc. Spec. Publ., 110*.

De Blasio, F. V. (2011), The aureole of Olympus Mons (Mars) as the compound deposit of submarine landslides, *Earth Planet. Sci. Lett.*, *312*, 126–139, doi:10.1016/j.epsl.2011.09.019.

Delcamp, A., B. van Wyk de Vries, and M. R. James (2008), The influence of edifice slope and substrata on volcano spreading, *J. Volcanol. Geotherm. Res.*, *177*, 925–943, doi:10.1016/j.jvolgeores.2008.07.014.

Dzurisin, D. (2007), *Volcano Deformation*, 1st ed., Springer, Berlin.

Francis, P. W., and G. Wadge (1983), The Olympus Mons aureole—Formation by gravitational spreading, *J. Geophys. Res.*, *88*, 8333–8344, doi:10.1029/JB088iB10p08333.

Freed, A. M., H. J. Melosh, and S. C. Solomon (2001), Tectonics of mascon loading: Resolution of the strike-slip faulting paradox, *J. Geophys. Res.*, *106*(E9), 20,603–20,620, doi:10.1029/2000JE001347.

Harris, S. A. (1977), The aureole of Olympus Mons, Mars, *J. Geophys. Res.*, *82*, 3099–3107, doi:10.1029/JB082i020p03099.

Hartmann, W. K., and G. Neukum (2001), Cratering chronology and the evolution of Mars, *Space Sci. Rev.*, *96*, 165–194.

Hiller, K. H., G. P. O. Neukum, P. Janle, J. E. Guest, and R. M. C. Lopes (1982), Mars—Stratigraphy and gravimetry of Olympus Mons and its aureole, *J. Geophys. Res.*, *87*, 9905–9915, doi:10.1029/JB087iB12p09905.

Hoek, E., and E. T. Brown (1998), Practical estimates of rock mass strength, *Int. J. Rock Mech. Min. Sci.*, *34*, 1165–1186.

Hubbert, M. K., and W. W. Rubey (1959), Role of fluid pressure in mechanics of overthrust faulting, *Geol. Soc. Am. Bull.*, *70*, 115–206.

Isherwood, R. J., L. M. Jozwiak, J. C. Jansen, and J. C. Andrews-Hanna (2013), The volcanic history of Olympus Mons from paleo-topography and flexural modeling, *Earth Planet. Sci. Lett.*, *363*, 88–96, doi:10.1016/j.epsl.2012.12.020.

Karato, S., and P. Wu (1993), Rheology of the upper mantle: A synthesis, *Science*, *260*(5109), 771–778, doi:10.1126/science.260.5109.771.

Krantz, R. W. (1988), Multiple fault sets and three-dimensional strain: Theory and application, *J. Struct. Geol.*, *10*(3), 225–237, doi:10.1016/0191-8141(88)90056-9.

Le Corvec, N., and T. R. Walter (2009), Volcano spreading and fault interaction influenced by rift zone intrusions: Insights from analogue experiments analyzed with digital image correlation technique, *J. Volcanol. Geotherm. Res.*, *183*, 170–182, doi:10.1016/j.jvolgeores.2009.02.006.

Le Corvec, N., T. R. Walter, J. Ruch, A. Bonforte, and G. Puglisi (2014), Experimental study of the interplay between magmatic rift intrusion and flank instability with application to the 2001 Mount Etna eruption, *J. Geophys. Res.*, *119*(7), 5356–5368, doi:10.1002/2014JB011224.

Lopes, R., K. Hiller, G. Neukum, and J. E. Guest (1982), Further evidence for a mass movement origin of the Olympus Mons aureole, *J. Geophys. Res.*, *87*, 9917–9928, doi:10.1029/JB087iB12p09917.

Lopes, R. M. C., J. E. Guest, and C. J. Wilson (1980), Origin of the Olympus Mons aureole and perimeter scarp, *Moon Planets*, *22*, 221–234, doi:10.1007/BF00898433.

Lund, B. (2005), Effects of deglaciation on the crustal stress field and implications for endglacial faulting: A parametric study of simple Earth and ice models, *Tech. Rep. TR-05-04*, Uppsala Univ., Sweden.

McGovern, P. J., and J. K. Morgan (2009), Volcanic spreading and lateral variations in the structure of Olympus Mons, Mars, *Geology*, *37*, 139–142.

McGovern, P. J., and S. C. Solomon (1993), State of stress, faulting, and eruption characteristics of large volcanoes on Mars, *J. Geophys. Res.*, *98*, 23,553–23,579, doi:10.1029/93JE03093.

McGovern, P. J., S. C. Solomon, D. E. Smith, M. T. Zuber, M. Simons, M. A. Wieczorek, R. J. Phillips, G. A. Neumann, O. Aharonson, and J. W. Head (2002), Localized gravity/topography admittance and correlation spectra on Mars: Implications for regional and global evolution, *J. Geophys. Res.*, *107*(E12), 5136, doi:10.1029/2002JE001854.

McGovern, P. J., J. R. Smith, J. K. Morgan, and M. H. Bulmer (2004a), Olympus Mons aureole deposits: New evidence for a flank failure origin, *J. Geophys. Res.*, *109*, E08008, doi:10.1029/2004JE002258.

McGovern, P. J., S. C. Solomon, D. E. Smith, M. T. Zuber, M. Simons, M. A. Wieczorek, R. J. Phillips, G. A. Neumann, O. Aharonson, and J. W. Head (2004b), Correction to "Localized gravity/topography admittance and correlation spectra on Mars: Implications for regional and global evolution", *J. Geophys. Res.*, *109*, E07007, doi:10.1029/2004JE002286.

McGovern, P. J., E. B. Grosfils, G. A. Galgana, J. K. Morgan, M. E. Rumpf, J. R. Smith, and J. R. Zimbelman (2014), Lithospheric flexure and volcano basal boundary conditions: Keys to the structural evolution of large volcanic edifices on the terrestrial planets, in *Volcanism and Tectonism Across the Inner Solar System*, vol. 401, edited by T. Platz et al., *Geol. Soc. London, Spec. Publ., 401*, 219–237.

Merle, O., and A. Borgia (1996), Scaled experiments of volcanic spreading, *J. Geophys. Res.*, *101*, 13,805–13,818, doi:10.1029/95JB03736.

Morgan, J. K., and P. J. McGovern (2005), Discrete element simulations of gravitational volcanic deformation: 1. Deformation structures and geometries, *J. Geophys. Res.*, *110*, B05402, doi:10.1029/2004JB003252.

Morris, E. C., and K. L. Tanaka (1994), *Atlas of Mars: Olympus Mons Region*, Geol. Inv. Series I-2327, U.S. Geological Survey, Denver.

Musiol, S. (2013), Geodynamics of the volcanoes Hadriaca Patera and Olympus Mons on Mars—Synthesis of observations and finite element modeling, PhD thesis, Fachbereich Geowissenschaften, Freie Universität Berlin.

Neukum, G., et al. (2004), Recent and episodic volcanic and glacial activity on Mars revealed by the High Resolution Stereo Camera, *Nature*, *432*, 971–979, doi:10.1038/nature03231.

Neumann, G. A., M. T. Zuber, M. A. Wieczorek, P. J. McGovern, F. G. Lemoine, and D. E. Smith (2004), Crustal structure of Mars from gravity and topography, *J. Geophys. Res.*, *109*, E08002, doi:10.1029/2004JE002262.

Oehler, J. F., B. van Wyk de Vries, and P. Labazuy (2005), Landslides and spreading of oceanic hot-spot and arc shield volcanoes on Low Strength Layers (LSLs): An analogue modeling approach, *J. Volcanol. Geotherm. Res.*, *144*, 169–189.

Platz, T., G. Michael, K. L. Tanaka, J. A. Skinner Jr., and C. M. Fortezzo (2013), Crater-based dating of geological units on Mars: Methods and application for the new global geological map, *Icarus*, *225*(1), 806–827, doi:10.1016/j.icarus.2013.04.021.

Plescia, J. B. (2004), Morphometric properties of Martian volcanoes, *J. Geophys. Res.*, *109*, E03003, doi:10.1029/2002JE002031.

Pullan, S., and K. Lambeck (1981), Mascons and loading of the lunar lithosphere, in *Proc. Lunar Planet. Sci. Conf.*, vol. 12, edited by Lunar Planet. Inst., pp. 853–865, Houston, Tex.

Schultz, R. A. (1995), Limits on strength and deformation properties of jointed basaltic rock masses, *Rock Mech. Rock Engng.*, *28*, 1–15.

Schultz, R. A., and M. T. Zuber (1994), Observations, models, and mechanisms of failure of surface rocks surrounding planetary surface loads, *J. Geophys. Res.*, *99*(E7), 14,691–14,702, doi:10.1029/94JE01140.

Tanaka, K. L. (1985), Ice-lubricated gravity spreading of the Olympus Mons aureole deposits, *Icarus*, *62*, 191–206, doi:10.1016/0019-1035(85)90117-4.

Tanaka, K. L., J. A. Skinner Jr., J. M. Dohm, R. P. Irwin III, E. J. Kolb, C. M. Fortezzo, T. Platz, G. G. Michael, and T. M. Hare (2014), *Geologic Map of MarsSci. Inv. Map 3292, 3292*, Denver, Colo.

Thomas, P. J., S. W. Squyres, and M. H. Carr (1990), Flank tectonics of Martian volcanoes, *J. Geophys. Res.*, *95*, 14,345–14,355, doi:10.1029/JB095iB09p14345.

Thurber, C. H., and M. N. Toksöz (1978), Martian lithospheric thickness from elastic flexure theory, *Geophys. Res. Lett.*, *5*, 977–980, doi:10.1029/GL005i011p00977.

Turcotte, D. L., and G. Schubert (2002), *Geodynamics*, 2nd ed., 456 pp., Cambridge Univ. Press, Cambridge.

Turcotte, D. L., R. J. Willemann, W. F. Haxby, and J. Norberry (1981), Role of membrane stresses in the support of planetary topography, *J. Geophys. Res.*, *86*(B5), 3951–3959, doi:10.1029/JB086iB05p03951.

van Wyk de Vries, B., and P. W. Francis (1997), Catastrophic collapse at stratovolcanoes induced by gradual volcano spreading, *Nature*, *387*, 387–390.

van Wyk de Vries, B., S. Self, P. W. Francis, and L. Keszthelyi (2001), A gravitational spreading origin for the Socompa debris avalanche, *J. Volcanol. Geotherm. Res.*, *105*, 225–247.

Williams, C. A., and R. M. Richardson (1991), A rheologically layered three-dimensional model of the San Andreas Fault in central and southern California, *J. Geophys. Res.*, *96*, 16,597–16,623.

Wu, P. (1992), Deformation of an incompressible viscoelastic flat earth with powerlaw creep: A finite element approach, *Geophys. J. Int.*, *108*, 35–51.

Wu, P. (2004), Using commercial finite element packages for the study of earth deformations, sea levels and the state of stress, *Geophys. J. Int.*, *158*, 401–408, doi:10.1111/j.1365-246X.2004.02338.x.

Zucca, J. J., D. P. Hill, and R. L. Kovach (1982), Crustal structure of Mauna Loa Volcano, Hawaii, from seismic refraction and gravity data, *Bull. Seismol. Soc. Am.*, *72*(5), 1535–1550.